Scattered spectra from inverse Compton sources operating at high laser fields and high electron energies

G. A. Krafft,[1,2] B. Terzić,[2,*] E. Johnson,[2] and G. Wilson[3]

[1]*Thomas Jefferson National Accelerator Facility, Newport News, Virginia 23606, USA*
[2]*Department of Physics, Center for Accelerator Science, Old Dominion University, Norfolk, Virginia 23529, USA*
[3]*Department of Mathematics, Regent University, Virginia Beach, Virginia 23464, USA*

(Received 28 June 2022; accepted 23 February 2023; published 28 March 2023)

As Compton x-ray and gamma-ray sources become more prevalent, to understand their performance in a precise way, it becomes important to be able to compute the distribution of scattered photons precisely. For example, codes have been developed at Old Dominion University which were used to understand the performance of the Dresden Compton Source in detail. An ideal model would (i) include the full Compton effect frequency relations between incident and scattered photons, (ii) allow the field strength to be large enough that nonlinear effects are captured, and (iii) allow the effects of electron beam emittance to be introduced and studied. Various authors have considered various pieces of this problem, but until now, no analytical or numerical procedure is known to us that captures these three effects simultaneously. Here we present a model for spectrum calculations which simultaneously cover these aspects. The model is compared to a published full quantum mechanical calculation and found to agree for a case where both full Compton effect and nonlinear field strength are present. We use this model to investigate chirping prescriptions to mitigate ponderomotive broadening.

DOI: 10.1103/PhysRevAccelBeams.26.034401

I. INTRODUCTION

Inverse Compton sources (ICS) are emerging as preferred sources of radiation in the intermediate regimes either not covered by other high-brilliance sources (synchrotron light sources and free electron lasers) or when applications require compactness and portability so that they can be used in hospitals, labs, universities, homeland security, and other fields [1–3]. Because of their superior spectral densities and narrow bandwidths, ICS are being used as γ-ray sources in nuclear photonics, photonuclear, and fundamental physics [4–7]. Optimizing the performance of these ICS requires accurate theoretical understanding and their computational implementation for all regimes of operation including the nonlinear regime at high incident laser field intensity and the so-called Compton regime where quantum mechanical electron recoil is fully accounted for.

One approach to perform such calculations is with the code CAIN [8], in which both the electron beam and photon beam are treated as ensembles of particles. The resulting scattered distribution is computed quantum mechanically by integrating over the relevant distributions. An advantage of such an approach is that nonlinear (due to the high laser field intensity) effects on the scattered distribution can be captured in the calculation. However, as discussed in Refs. [9,10], by virtue of CAIN's Monte Carlo algorithm and the way it simulates physical effects, the rare events in nature will be as rare in the simulation. This means that the statistics in situations where low scattered photon counts are expected—for example, in the tails of the distribution or at very narrow apertures—will suffer from poor statistics. In contrast, the new model introduced here computes scattering probabilities—the likelihood of scattered photons to be found in each portion of the spectrum, leading to the same accuracy in each portion of the spectrum. Additionally, CAIN simulations cannot feature different laser shapes, nor can they capture arbitrary laser chirping. These features are available in the new model presented here.

Early analytical and numerical formalisms for a single-electron back-scattering off a high-intensity laser field modeled by a 1D plane wave in which electron recoil is neglected (nonlinear Thomson regime) were developed for a constant laser envelope [11] and then for general non-constant envelope shapes in Refs. [12–15]. The study of nonconstant envelope shapes led to the discovery of ponderomotive spectral broadening which is so deleterious that most ICS either remain at low laser intensities or pay a

*bterzic@odu.edu

steep price to operate at a small fraction of the physically possible peak spectral output [14]. This ponderomotive broadening can be almost completely corrected and eliminated by suitable frequency modulation (FM; chirping) of the incident laser pulse in both the nonlinear Thomson regime (at low-to-medium electron energies when electron recoil can be neglected) [16–19] and the nonlinear Compton regime (at high electron energies when electron recoil is accounted for) [20,21]. While the treatment of the scattered spectra in the Compton regime is semiclassical, it perfectly agrees with QED derivation presented in Refs. [21,22].

The novel calculation presented in this work has been developed into a computational model that simulates ICS spectra incident upon a sensor aperture of arbitrary size and placement. This new model, NLCS, captures both the full nonlinear effects indicative of a high-intensity laser pulse, i.e., ponderomotive broadening, the onset of harmonics and subsidiary peaks, etc., and also the Compton effects that arise from electron recoil. Earlier computational models have used an application of Larmor's radiation formula combined with a Fourier to transform to develop great insight into the scaling laws of ICS spectra; these previous models do not, however, capture nonlinear and Compton effects simultaneously. These earlier calculations are also far less general: the range of parameters for which they are valid is quite limited [23,24]. Other semiclassical calculations have been developed to simulate nonlinear Compton spectra by using the Baër-Katkov (BK) approximation [25–27] or the Wentzel-Kramers-Brillouin (WKB) model [28,29]. The particle-in-cell (PIC) method has been used to introduce QED corrections to classical calculations [30,31]. Fully quantum calculations have been also derived from nonperturbative QED utilizing Volkov states [21,22,32]. These approaches have produced several powerful computational models to simulate emitted radiation from synchrotrons, laser-plasma accelerators, and ICS. The model that we present here, however, stands out from other ICS simulations due to the generalized treatment of both the electron beam and the laser pulse: each particle is treated with its own six-dimensional coordinates and the incident laser envelope may have

TABLE I. Comparison of the physics captured by prominent photon-electron scattering calculations. The symbol ✓* indicates that the calculation accounts for the angular distribution of the scattered photon energy without demonstrating the aperture effect on the spectral distribution.

Scattering calculation	Compton recoil	Nonlinear effects	Emittance	Transverse laser size pulse	Ultra-short pulse	Chirping	ICS spectrum through aperture
NLCS	✓	✓	✓	✓	✓	✓	✓
CAIN	✓	✓	✓	✓	✓	×	✓
SENSE	×	✓	✓	✓	✓	✓	✓
NLTX	×	✓	✓	✓	✓	✓	✓
ICCS	✓	×	✓	✓	✓	✓	✓
Esarey [11]	×	✓	✓	×	✓	×	✓*
Hartemann [12]	×	✓	×	✓	✓	×	×
Hartemann [13]	×	✓	×	✓	✓	×	×
Krafft [14]	×	✓	×	×	✓	×	×
Brau [15]	×	✓	×	×	✓	×	×
Gheb [16]	×	✓	×	×	×	✓	×
Terzić [17]	×	✓	×	×	✓	✓	×
Rykovanov [18]	×	✓	×	×	✓	✓	×
Terzić [19]	×	✓	×	×	✓	✓	×
Terzić [20]	✓	✓	✓	×	✓	✓	×
Maroli [34]	✓	✓	×	×	✓	✓	✓
Seipt [21]	✓	✓	×	×	✓	✓	✓
Seipt [22]	✓	✓	×	×	✓	×	×
Albert [23]	✓	✓	✓	✓	×	×	×
Hartemann [24]	✓	✓	✓	×	✓	×	✓*
Ridgers [25]	✓	✓	×	×	×	×	×
Artru [26]	✓	✓	×	×	×	×	×
Li [27]	✓	✓	×	×	×	×	×
Piazza [28]	✓	✓	×	×	×	×	×
Piazza [29]	✓	✓	×	×	×	×	×
Gonoskov [30]	×	✓	×	×	×	×	×
Vranic [31]	×	✓	×	×	×	×	×
Mackenroth [32]	✓	✓	×	×	×	×	×
Mackenroth [35]	×	✓	×	✓	×	×	✓*

any envelope shape. Furthermore, the incident laser pulse can optionally be programmed to simulate any FM (chirping) function to correct for ponderomotive broadening. Table I shows a comparison of ICS models that are similar to NLCS, including our earlier nonlinear Thomson codes SENSE [10] and NLTX [33] and linear Compton code ICCS. Our model applies in the regime where the laser pulse length is short compared to the Rayleigh range of the laser focus, so diffraction effects are negligible.

The paper is organized as follows: In Sec. II, we present the equations underpinning our new nonlinear inverse Compton scattering model, including the recovery of linear Compton and nonlinear Thomson as limiting cases. In Sec. III, we use the code based on the new formalism to compute spectra of ICS operating in the nonlinear Compton regime; the advantages afforded by longitudinal laser chirping are clearly illustrated. Finally, in Sec. IV, we conclude.

II. NONLINEAR INVERSE COMPTON SCATTERING MODEL

A step toward simulating a realistic ICS was taken after generalizing these approaches for an on-axis single-electron backscattering into codes for the computation of scattered spectra from an entire electron distribution with an energy spread and emittance into a finite aperture for the nonlinear Thomson regime [10,33,36] and for the linear Compton regime [9,37]. These codes were shown to be in excellent agreement with other codes and experimental results, such as those from the Dresden Compton Source [10]. Here we present a formalism that unifies and subsumes these two formalisms—nonlinear Thomson and linear Compton—into a heretofore unexplored nonlinear Compton regime in which nonlinearities arise due to both high laser field intensities and electron recoil. Including electron emittance and electron energy spread effects in strong-field QED spectral calculations [22], if executed, could provide an alternate means of calculating the new results presented here.

In order to allow the widest applicability of our results, we allow completely arbitrary incident electron and linearly or circularly polarized photon conditions. First, the model is constructed out of plane waves; later, we indicate modifications that can successfully capture effects such as transversely varying intensities. Our notation will follow closely that found in Ref. [37] on linear Compton scattering. First define notation: all quantities in this paper are in the lab frame. The incident plane-wave vector potential is $A(\xi)\boldsymbol{\varepsilon}$ with $\xi = (ct - \hat{\boldsymbol{k}}\cdot\boldsymbol{x})$ and with $\boldsymbol{\varepsilon}\cdot\boldsymbol{k} = 0$. The incident laser propagation four-vector is thus $\omega(1,\hat{\boldsymbol{k}})$ with ω the frequency in the incident photon beam. The relativistic four-momentum of the individual electron is $(\gamma,\gamma\boldsymbol{\beta})mc$. Using standard conventions, the scattered propagation four-vector is $\omega'(1,\hat{\boldsymbol{k}}')$ with ω' the scattered frequency and assuming the scattered radiation polarization vector is $\boldsymbol{\varepsilon}'$. As in Ref. [37], the general formula relating the scattered frequency to the incident frequency including the full Compton effect is

$$\omega'(\omega) = \frac{\omega(1-\boldsymbol{\beta}\cdot\hat{\boldsymbol{k}})}{1-\boldsymbol{\beta}\cdot\hat{\boldsymbol{k}}' + \frac{\hbar\omega}{\gamma m_e c^2}(1-\hat{\boldsymbol{k}}\cdot\hat{\boldsymbol{k}}')}, \tag{1}$$

with inverse relation

$$\omega(\omega') = \frac{\omega'(1-\boldsymbol{\beta}\cdot\hat{\boldsymbol{k}}')}{1-\boldsymbol{\beta}\cdot\hat{\boldsymbol{k}} - \frac{\hbar\omega'}{\gamma m_e c^2}(1-\hat{\boldsymbol{k}}\cdot\hat{\boldsymbol{k}}')}. \tag{2}$$

For linear polarization, the scattered energy distribution for linear Compton scattering is

$$\frac{\mathrm{d}^2E'}{\mathrm{d}\omega'\mathrm{d}\Omega} = \frac{\epsilon_0}{2\pi c}|\tilde{E}(\omega(\omega')/c)|^2\frac{\mathrm{d}\sigma}{\mathrm{d}\Omega}\left[\frac{\omega'}{\omega}\frac{\mathrm{d}\omega}{\mathrm{d}\omega'}\right], \tag{3}$$

where E' is the scattered energy, ϵ_0 is the permittivity of free space, and $\tilde{E}(k) = -\omega\tilde{A}(k)$ is the spatial Fourier transform of the electric field; where the scattering cross section into the scattered polarization $\boldsymbol{\varepsilon}'$ is the Klein-Nishina cross section

$$\frac{\mathrm{d}\sigma}{\mathrm{d}\Omega} = \frac{r_e^2}{\gamma^2(1-\boldsymbol{\beta}\cdot\hat{\boldsymbol{k}})^2}\left(\frac{\omega'}{\omega}\right)^2\left[\frac{\omega'(1-\boldsymbol{\beta}\cdot\hat{\boldsymbol{k}}')}{4\omega(1-\boldsymbol{\beta}\cdot\hat{\boldsymbol{k}})} + \frac{\omega(1-\boldsymbol{\beta}\cdot\hat{\boldsymbol{k}})}{4\omega'(1-\boldsymbol{\beta}\cdot\hat{\boldsymbol{k}}')} - \frac{1}{2} + [\boldsymbol{\varepsilon}_b\cdot\boldsymbol{\varepsilon}_b']^2\right], \tag{4}$$

and r_e is the classical electron radius; and where

$$\boldsymbol{\varepsilon}_b\cdot\boldsymbol{\varepsilon}_b' = \boldsymbol{\varepsilon}\cdot\boldsymbol{\varepsilon}' + \frac{(\boldsymbol{\beta}\cdot\boldsymbol{\varepsilon})(\hat{\boldsymbol{k}}\cdot\boldsymbol{\varepsilon}')}{(1-\boldsymbol{\beta}\cdot\hat{\boldsymbol{k}})} + \frac{(\boldsymbol{\beta}\cdot\boldsymbol{\varepsilon}')(\hat{\boldsymbol{k}}'\cdot\boldsymbol{\varepsilon})}{(1-\boldsymbol{\beta}\cdot\hat{\boldsymbol{k}}')} + \frac{(\boldsymbol{\beta}\cdot\boldsymbol{\varepsilon})(\boldsymbol{\beta}\cdot\boldsymbol{\varepsilon}')}{(1-\boldsymbol{\beta}\cdot\hat{\boldsymbol{k}})(1-\boldsymbol{\beta}\cdot\hat{\boldsymbol{k}}')}(\hat{\boldsymbol{k}}\cdot\hat{\boldsymbol{k}}'-1). \tag{5}$$

Equation (5) does not appear explicitly in Ref. [37] but may be derived directly by computing $\hat{\boldsymbol{k}}\cdot\hat{\boldsymbol{k}}' - 1$ using Eq. (15) and inserting in Eq. (17) or by expanding the four-scalar products in Eq. (18) there.

Similarly, calculations of nonlinear Thomson spectra [14] have been recently completed with arbitrary electron and incident photon initial conditions in Ref. [33]. The result for the spectrum into the general polarization $\boldsymbol{\varepsilon}'$, after converting to notation here, is

$$\frac{\mathrm{d}^2 E'_{\boldsymbol{\varepsilon}'}}{\mathrm{d}\omega' \mathrm{d}\Omega} = \frac{e^2\omega'^2}{32\pi^3\epsilon_0 c^3}\left| D_1(\omega'')(\boldsymbol{\varepsilon}\cdot\boldsymbol{\varepsilon}') + D_1(\omega'')\frac{\boldsymbol{\beta}\cdot\boldsymbol{\varepsilon}}{(1-\boldsymbol{\beta}\cdot\hat{\mathbf{k}})}(\hat{\mathbf{k}}\cdot\boldsymbol{\varepsilon}') - D_2(\omega'')(\hat{\mathbf{k}}\cdot\boldsymbol{\varepsilon}') \right.$$
$$\left. - \frac{[(\boldsymbol{\beta}\cdot\boldsymbol{\varepsilon})(1-\hat{\mathbf{k}}\cdot\hat{\mathbf{k}}')/(1-\boldsymbol{\beta}\cdot\hat{\mathbf{k}}) - (\hat{\mathbf{k}}'\cdot\boldsymbol{\varepsilon})]D_1(\omega'') - (1-\hat{\mathbf{k}}\cdot\hat{\mathbf{k}}')D_2(\omega'')}{1-\boldsymbol{\beta}\cdot\hat{\mathbf{k}}'}\boldsymbol{\beta}\cdot\boldsymbol{\varepsilon}' \right|^2, \tag{6}$$

where

$$D_1(\omega';\theta,\varphi) = \frac{1}{\gamma(1-\boldsymbol{\beta}\cdot\hat{\mathbf{k}})}\int \tilde{A}(\xi')e^{i\Phi(\xi')}\mathrm{d}\xi'$$
$$D_2(\omega';\theta,\varphi) = \frac{1}{\gamma^2(1-\boldsymbol{\beta}\cdot\hat{\mathbf{k}})^2}\int \frac{\tilde{A}^2(\xi')}{2}e^{i\Phi(\xi')}\mathrm{d}\xi'$$
$$\Phi(\xi') = \frac{\omega'}{c}\begin{pmatrix} \xi'\frac{(1-\boldsymbol{\beta}\cdot\hat{\mathbf{k}}')}{(1-\boldsymbol{\beta}\cdot\hat{\mathbf{k}})} \\ -\left[\frac{\boldsymbol{\beta}\cdot\boldsymbol{\varepsilon}}{(1-\boldsymbol{\beta}\cdot\hat{\mathbf{k}})}(1-\hat{\mathbf{k}}\cdot\hat{\mathbf{k}}') - \hat{\mathbf{k}}'\cdot\boldsymbol{\varepsilon}\right]\int_{-\infty}^{\xi'}\frac{\tilde{A}(\xi'')}{\gamma(1-\boldsymbol{\beta}\cdot\hat{\mathbf{k}})}\mathrm{d}\xi'' \\ +(1-\hat{\mathbf{k}}\cdot\hat{\mathbf{k}}')\int_{-\infty}^{\xi'}\frac{\tilde{A}^2(\xi'')}{2\gamma^2(1-\boldsymbol{\beta}\cdot\hat{\mathbf{k}})^2}\mathrm{d}\xi'' \end{pmatrix}, \tag{7}$$

$\tilde{A} = qA/mc$ is the normalized vector potential, and ω'' is defined in a moment. Examining the terms in Eq. (6) closely, notice that the terms proportional to D_1 within the complex square exactly correspond to the elements of the linear cross section on the right-hand side of Eq. (5). One can make a general nonlinear Compton theory by replacing $\boldsymbol{\varepsilon}_b\cdot\boldsymbol{\varepsilon}'_b$ in the linear Compton result with the full nonlinear expressions in Eq. (6), as long as one can make sure the $\tilde{E}$ and $\tilde{D}_1$ can be made to agree for a suitable choice of arguments.

Two approaches can be used to determine the proper argument to place in the D functions. The first is simply to require that the general theory reduce the linear Compton result at low field strengths, as is verified below. The second justification, more in keeping with the original derivation of the linear Compton theory [37], is to determine expressions for the D functions as a function of incident frequency, and as in the linear Compton theory, simply replace all instances of ω in the formula with $\omega(\omega')$ as given in Eq. (2).

In terms of the incident frequency, the D functions within nonlinear Thomson theory become

$$D_1(\omega;\theta,\varphi) = \frac{1}{\gamma(1-\boldsymbol{\beta}\cdot\hat{\mathbf{k}})}\int \tilde{A}(\xi')e^{i\Phi(\xi')}\mathrm{d}\xi'$$
$$D_2(\omega;\theta,\varphi) = \frac{1}{\gamma^2(1-\boldsymbol{\beta}\cdot\hat{\mathbf{k}})^2}\int \frac{\tilde{A}^2(\xi')}{2}e^{i\Phi(\xi')}\mathrm{d}\xi'$$
$$\Phi(\xi') = \frac{\omega}{c}\begin{pmatrix} \xi' \\ -\frac{(1-\boldsymbol{\beta}\cdot\hat{\mathbf{k}})}{(1-\boldsymbol{\beta}\cdot\hat{\mathbf{k}}')}\left[\frac{\boldsymbol{\beta}\cdot\boldsymbol{\varepsilon}}{(1-\boldsymbol{\beta}\cdot\hat{\mathbf{k}})}(1-\hat{\mathbf{k}}\cdot\hat{\mathbf{k}}') - \hat{\mathbf{k}}'\cdot\boldsymbol{\varepsilon}\right]\int_{-\infty}^{\xi'}\frac{\tilde{A}(\xi'')}{\gamma(1-\boldsymbol{\beta}\cdot\hat{\mathbf{k}})}\mathrm{d}\xi'' \\ +\frac{(1-\boldsymbol{\beta}\cdot\hat{\mathbf{k}})}{(1-\boldsymbol{\beta}\cdot\hat{\mathbf{k}}')}(1-\hat{\mathbf{k}}\cdot\hat{\mathbf{k}}')\int_{-\infty}^{\xi'}\frac{\tilde{A}^2(\xi'')}{2\gamma^2(1-\boldsymbol{\beta}\cdot\hat{\mathbf{k}})^2}\mathrm{d}\xi'' \end{pmatrix}. \tag{8}$$

Replacing ω by $\omega(\omega')$ and re-expressing the phase integral in terms of the original expression, one obtains

$$\Phi(\xi') = \frac{\omega(\omega')}{c}\frac{(1-\boldsymbol{\beta}\cdot\hat{\boldsymbol{k}})}{(1-\boldsymbol{\beta}\cdot\hat{\boldsymbol{k}}')}\left(\begin{array}{c} \xi'\frac{(1-\boldsymbol{\beta}\cdot\hat{\boldsymbol{k}}')}{(1-\boldsymbol{\beta}\cdot\hat{\boldsymbol{k}})} \\ -\left[\frac{\boldsymbol{\beta}\cdot\boldsymbol{\varepsilon}}{(1-\boldsymbol{\beta}\cdot\hat{\boldsymbol{k}})}(1-\hat{\boldsymbol{k}}\cdot\hat{\boldsymbol{k}}')-\hat{\boldsymbol{k}}'\cdot\boldsymbol{\varepsilon}\right]\int_{-\infty}^{\xi'}\frac{\tilde{A}(\xi'')}{\gamma(1-\boldsymbol{\beta}\cdot\hat{\boldsymbol{k}})}\mathrm{d}\xi'' \\ +(1-\hat{\boldsymbol{k}}\cdot\hat{\boldsymbol{k}}')\int_{-\infty}^{\xi'}\frac{\tilde{A}^2(\xi'')}{2\gamma^2(1-\boldsymbol{\beta}\cdot\hat{\boldsymbol{k}})^2}\mathrm{d}\xi'' \end{array}\right). \tag{9}$$

From this expression, the modification for constructing the general nonlinear Compton theory follows. The input frequencies to the D functions should be Compton shifted from the input frequencies in the Thomson nonlinear theory [20]. From Eqs. (2) and (9), the general shift formula is

$$\omega'' = \frac{\omega(1-\boldsymbol{\beta}\cdot\hat{\boldsymbol{k}})}{1-\boldsymbol{\beta}\cdot\hat{\boldsymbol{k}}'} = \frac{\omega'(1-\boldsymbol{\beta}\cdot\hat{\boldsymbol{k}})}{1-\boldsymbol{\beta}\cdot\hat{\boldsymbol{k}}-\frac{\hbar\omega'}{\gamma m_e c^2}(1-\hat{\boldsymbol{k}}\cdot\hat{\boldsymbol{k}}')}, \tag{10}$$

with the shifted frequency being placed into the argument of the phase integrals when evaluating the D functions. It reduces to the Thomson result in the Thomson limit as $\omega'' \to \omega'$ when $\hbar = 0$ in Eq. (10).

To summarize, the energy scattered by a single electron in the new nonlinear Compton scattering model is

$$\frac{\mathrm{d}^2E'_{\mathrm{tot}}}{\mathrm{d}\omega'\mathrm{d}\Omega} = \left[\frac{e^2\omega'^2}{32\pi^3\epsilon_0 c^3}|D_1(\omega'')|^2\left(\frac{\omega'(1-\boldsymbol{\beta}\cdot\hat{\boldsymbol{k}}')}{2\omega(1-\boldsymbol{\beta}\cdot\hat{\boldsymbol{k}})}+\frac{\omega(1-\boldsymbol{\beta}\cdot\hat{\boldsymbol{k}})}{2\omega'(1-\boldsymbol{\beta}\cdot\hat{\boldsymbol{k}}')}-1\right)+\frac{\mathrm{d}^2E'_{\boldsymbol{\varepsilon}'_\perp}}{\mathrm{d}\omega'\mathrm{d}\Omega}+\frac{\mathrm{d}^2E'_{\boldsymbol{\varepsilon}'_\parallel}}{\mathrm{d}\omega'\mathrm{d}\Omega}\right]\left[\frac{\omega'}{\omega}\frac{d\omega}{d\omega'}\right]. \tag{11}$$

The total scattered energy is obtained by incoherently summing this quantity over all the electrons in the beam. The first term in Eq. (11) gives the quantum correction to the scattering cross section in going from Thomson to Compton scattering. The second and third terms quantify the nonlinear scattering into two suitable transverse polarizations indicated here by $E'_{\boldsymbol{\varepsilon}'_\perp}$ and $E'_{\boldsymbol{\varepsilon}'_\parallel}$.

A fairly thorough discussion of the new model in the restricted case of perfect backscattering (the electron and incident photons perfectly antialigned), and with a more extensive discussion of frequency shifts and harmonic frequency values, appears in a recent publication [20].

A. Recovering appropriate limits

By its construction, the general model in Eq. (11) limits properly to the linear Compton theory and nonlinear Thomson theory. Automatically, $D_2 \ll D_1$ in the linear (small field strength) limit with $|\tilde{A}| \ll 1$. When $\tilde{A}$ integrates into something small, D_1 reduces to the Fourier transform of $\tilde{A}$. Specifically,

$$D_1(\omega'') \to \frac{\tilde{A}(\omega/c)}{\gamma(1-\boldsymbol{\beta}\cdot\hat{\boldsymbol{k}})} = -\frac{q\tilde{E}(\omega/c)}{mc\omega\gamma(1-\boldsymbol{\beta}\cdot\hat{\boldsymbol{k}})}. \tag{12}$$

In this circumstance, the general calculation leads back exactly to Eq. (3). This recovery of the nonlinear Thomson energy density spectrum is shown explicitly in Appendix A.

For the Thomson limit $\omega'' = \omega' = \omega(1-\boldsymbol{\beta}\cdot\hat{\boldsymbol{k}})/(1-\boldsymbol{\beta}\cdot\hat{\boldsymbol{k}}')$, the first term in Eq. (11) vanishes, and

$$\left[\frac{\omega'}{\omega}\frac{\mathrm{d}\omega}{\mathrm{d}\omega'}\right] = 1. \tag{13}$$

Thus, the general calculation in Eq. (11) exactly reproduces the results in Refs. [14,37] that it was built from. This recovery of the linear Compton energy density spectrum is shown explicitly in Appendix B.

B. Nonzero crossing angle

In the case of near-backscattering (the incident laser is aligned within an angle of $1/\gamma$ of perfect backscattering), the following generalization can be used to include a transverse dependence of the incident laser field. In computing, the scattering simply use $\tilde{A}(x,y)$ to compute the D functions, where (x,y) is the transverse offset of the electron as it passes the interaction point of the collision. Because the electron angles within the beam are small, the electron moves transversely a negligible amount as it passes through the laser pulse. On the other hand, for example, in 90° scattering, such a simple approach must be corrected because the electron moves by a significant amount transversely during the collision. The calculation of the D function must then include the change in the amplitude of $\tilde{A}$ as the electron moves through the laser pulse. This complication adds an additional integration to the spectrum calculation, which is not needed in the cases reported in this paper.

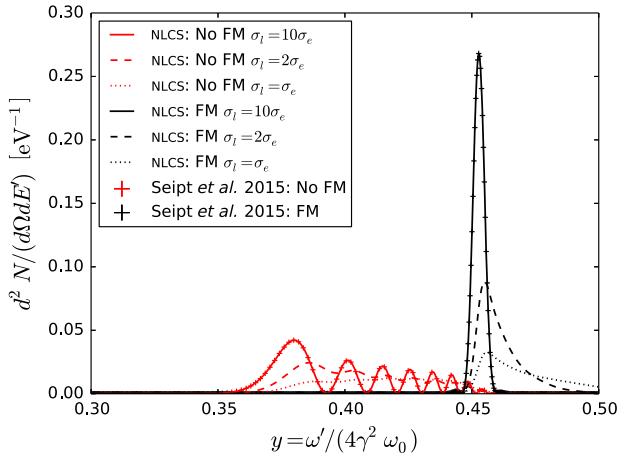

FIG. 1. Radiation spectra computed with our NLCS new code as the relative size of the laser waist (σ_l) compared to the electron beam waist (σ_e) is varied: significantly larger than ($\sigma_l = 10\sigma_e$; solid lines); somewhat larger than ($\sigma_l = 2\sigma_e$; dashed lines); and equal to ($\sigma_l = \sigma_e$; dotted lines) the electron beam waist. Uncompensated spectrum (no FM) shown in red lines and optimally compensated (FM) shown in black lines. The red and black crosses come from the top panel of Fig. 2 in Ref. [21]. Spectra shown are for a linearly polarized 800-nm laser with a pulse duration of 21 fs and $a_0 = 1$ on a Gaussian-distributed electron beam with a mean energy of 51 GeV.

C. Capturing the transverse laser pulse effects

The finite transverse extent of the laser pulse is modeled as detailed in Ref. [10]. Here we briefly summarize it for completeness.

The effective strength of the laser field, which an electron experiences, depends on the path it takes through the laser pulse. An on-axis electron experiences the maximum strength, a_0, while others "see" an effective strength attenuated by the amount commensurate to the electron closest transverse approach (x, y) to the center of the pulse: $a_{\text{eff}} = a_0 \exp(-x^2/\sigma_{l,x}^2 - y^2/\sigma_{l,y}^2)$, where $\sigma_{l,x}$ and $\sigma_{l,y}$ are horizontal and vertical rms size of the laser pulse, respectively. For each particle sampling the electron beam distribution, an inverse Compton-scattered spectrum is computed using the formalism that uses a 1D plane-wave model of the laser pulse, described earlier in this section. The transverse extent of the laser pulse is then captured by summing all of the computed spectra weighed by their effective strength of the laser field a_{eff}^2. The effects of the finite transverse waist of the laser pulse are shown in Fig. 1: as the relative size of the laser waist compared to the electron beam waist reduces, the peak spectral density drops, the structure smooths out and FM becomes less effective [10].

D. Frequency modulation function

Originally proposed by Ghebregziabher *et al.* [16], modulating the frequency (chirping) of the incident laser pulse increases brilliance in the scattered spectrum. In the plane-wave approximation, this chirping is defined by the function $f(\xi)$ which modifies the phase of the normalized incident laser pulse vector potential

$$\tilde{A}(\xi) = \frac{eA(\xi)}{mc} = a(\xi)\,\cos\left(\frac{2\pi\xi f(\xi)}{\lambda}\right), \tag{14}$$

where e is the electron charge, $\xi = z + ct$ is the coordinate along the laser pulse, $a(\xi)$ is the envelope of the vector potential, and λ is the wavelength of the incident photons. The optimal solution for any envelope shape in the plane-wave approximation may be found through the integral [17]

$$f(\xi) = \frac{1}{1 + a_0^2/2}\left(1 + \frac{\int_0^\xi a^2(\xi')\mathrm{d}\xi'}{2\xi}\right). \tag{15}$$

Optimized chirping prescriptions have also been developed for incident laser fields outside of the plane-wave approximation [10,38]. The shapes of exact FM functions for various laser envelopes are derived in Ref. [36] and plotted in Ref. [20]. Looking toward laser chirping shapes that are more easily realizable in the lab, recently, it has been shown that a simple saw-tooth chirping prescription leads to near-perfect recovery of narrow bandwidth and increased peak spectral density to within a few percent of the perfect compensation [33]. Even simpler (and more likely to be implemented experimentally), it has been shown recently that a substantial improvement in the peak spectral density in ICS can be achieved with just a linear chirp [39]. The computational models in the new code can simulate any general chirping prescription $f(\xi)$.

E. Circular polarization

The generalization to obtain nonlinear Compton scattering of a circularly polarized incident laser pulse can be found using the expression

$$\frac{\mathrm{d}^2E'}{\mathrm{d}\omega'\mathrm{d}\Omega} = \frac{e^2\omega'^2}{32\pi^3\epsilon_0 c^3}\left[\begin{array}{c}\left(\frac{\omega'(1-\boldsymbol{\beta}\cdot\hat{\boldsymbol{k}}')}{2\omega(1-\boldsymbol{\beta}\cdot\hat{\boldsymbol{k}})} + \frac{\omega(1-\boldsymbol{\beta}\cdot\hat{\boldsymbol{k}})}{2\omega'(1-\boldsymbol{\beta}\cdot\hat{\boldsymbol{k}}')} - 1\right)|D_1(\omega'')|^2 \\ +|D_1(\omega'')\frac{\boldsymbol{\beta}\cdot\boldsymbol{\varepsilon}}{(1-\boldsymbol{\beta}\cdot\hat{\boldsymbol{k}})}\mathbf{K} + D_1(\omega'')\mathbf{E} - D_2(\omega'')\mathbf{K} \\ -\frac{[(\boldsymbol{\beta}\cdot\boldsymbol{\varepsilon})(1-\hat{\boldsymbol{k}}\cdot\hat{\boldsymbol{k}}')-(1-\boldsymbol{\beta}\cdot\hat{\boldsymbol{k}})(\hat{\boldsymbol{k}}'\cdot\boldsymbol{\varepsilon})]D_1(\omega'')-(1-\boldsymbol{\beta}\cdot\hat{\boldsymbol{k}})(1-\hat{\boldsymbol{k}}\cdot\hat{\boldsymbol{k}}')D_2(\omega'')}{1-\boldsymbol{\beta}\cdot\hat{\boldsymbol{k}}'}\mathbf{P}|^2\end{array}\right] \times \left[\frac{\omega'}{\omega}\frac{\mathrm{d}\omega}{\mathrm{d}\omega'}\right], \tag{16}$$

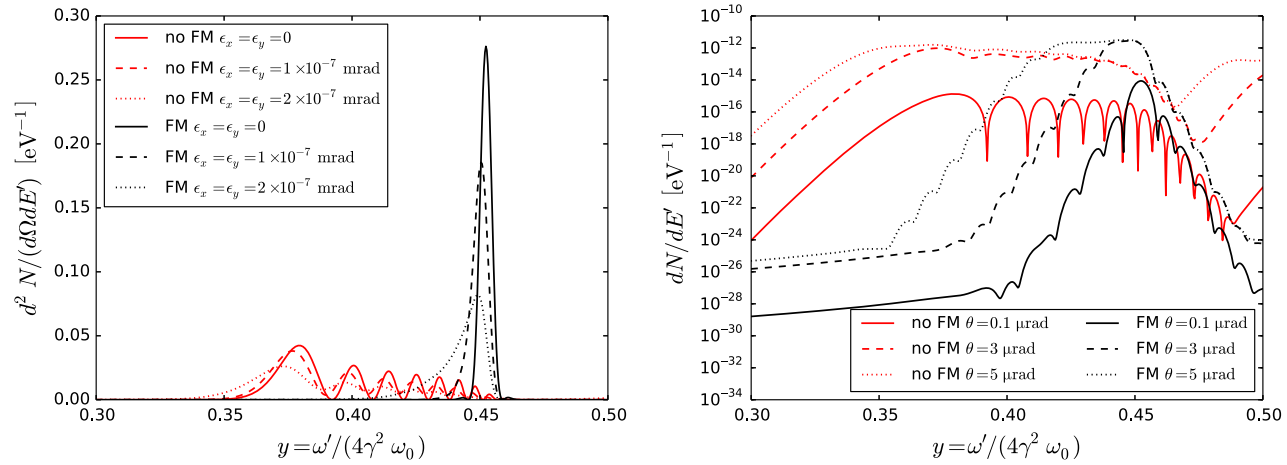

FIG. 2. Radiation spectrum for the nonlinear Compton scattering: uncompensated spectrum (no FM) is shown in red lines and optimally compensated (FM) in black. Left: Backscattered spectra ($d^2N/(d\Omega dE')$ for an electron beam with zero emittance (or for a single, on-axis particle) are shown in solid lines; $\varepsilon_x=\varepsilon_y=10^{-7}$ m rad emittance in dashed; and $\varepsilon_x=\varepsilon_y=2\times10^{-7}$ m rad emittance in dotted lines. Right: Spectra collected over a finite aperture, dN/dE', for an electron beam with zero emittance (or for a single, on-axis particle) and: $\theta=0.1$ μrad shown in solid lines; $\theta=3$ μrad shown in solid lines; $\theta=5$ μrad shown in solid lines. The solid red and black lines in both panels correspond to the same-colored lines in the top panel of Fig. 4 in Ref. [20] and the top panel of Fig. 2 in Ref. [21]. Spectra shown are for a linearly polarized 800-nm laser with pulse duration of 21 fs and $a_0=1$ on an Gaussian-distributed electron beam with mean energy of 51 GeV.

where $\mathbf{K}=(\hat{\boldsymbol{k}}'\cdot\hat{\boldsymbol{k}})\hat{\boldsymbol{k}}'-\hat{\boldsymbol{k}}$, $\mathbf{E}=(\hat{\boldsymbol{k}}'\cdot\boldsymbol{\varepsilon})\hat{\boldsymbol{k}}'-\boldsymbol{\varepsilon}$, and

$$\mathbf{P}=\frac{(\hat{\boldsymbol{k}}'\cdot\boldsymbol{p})\hat{\boldsymbol{k}}'-\boldsymbol{p}}{\sqrt{m^2c^2+\vec{p}\cdot\vec{p}}-\vec{p}\cdot\hat{k}}=\frac{(\hat{\boldsymbol{k}}'\cdot\boldsymbol{\beta})\hat{\boldsymbol{k}}'-\boldsymbol{\beta}}{(1-\boldsymbol{\beta}\cdot\hat{\boldsymbol{k}})}. \quad (17)$$

Once the integrals are computed to obtain the D functions, the various terms should be summed as indicated to form a vector quantity. This vector is dotted with its complex conjugate to obtain the final spectrum. One caution when calculating the circular polarized case, care must be taken to properly calculate the phases in the integrals when the D functions are evaluated. For example, when evaluating D_2 and the phases in the integrals, the vector potential squared no longer oscillates at the second harmonic frequency. The resulting harmonic generation is therefore entirely different between the linear polarization and circular polarization cases and must be calculated with a somewhat different code.

The formulas presented here are only for the perfectly polarized case. The model reported can be extended to an elliptically polarized laser beam. However, the expressions for the elliptically polarized case are more complicated and presently unknown.

F. NLCS code

The new code NLCS (Nonlinear Compton Spectra) implements the model described above. NLCS is a generalization of our nonlinear Thomson codes SENSE [10] and NLTX [33] to the nonlinear Compton regime. It computes the spectral energy density $d^2E'/(d\omega' d\Omega)$ [as well as the related spectral number density $d^2N/(d\omega' d\Omega)$] of the scattered radiation due to N_{part} individual simulation particles colliding with a laser pulse. The laser pulse is specified by an arbitrary longitudinal envelope $a(\xi)$ and a finite transverse rms size. That ensemble of simulation particles can be specified from an input file or randomly sampled from a phase-space distribution with specified rms properties. Monte Carlo integration over a solid angle $d\Omega(\theta,\phi)$ of the physical aperture with the angular size of θ_a is used to compute a spectrum $dE'(\omega')/d\omega'=\int d^2E(\omega';\Omega)/(d\omega' d\Omega)d\Omega$ for each of the N_{part} simulation particles sampling a distribution of N_e electrons. The total spectrum is the average of these individual spectra. NLCS is written in PYTHON and uses CYTHON and NUMPY for computational efficiency [40,41]. It is parallelized to run on multiple CPUs. All of the spectra reported in the next section are computed using NLCS.

Figures 1 and 2 illustrate the new functionalities of the NLCS code as compared to the formalism developed previously in Refs. [20,21]. Figure 1 shows the new code accounting for the finite transverse size of the laser pulse. The left panel of Fig. 2 illustrates the effects of the previously unaccounted for electron beam emittance: it broadens the spectra, smears out the structure, and makes FM less effective. The right panel of Fig. 2 shows the effects of spectra collected over a finite aperture (circular or rectangular), dN/dE', as opposed to the back-scattered case, $d^2N/(dE'd\Omega)$: increasing the aperture broadens the scattered spectra and makes FM less effective.

At a very high-field regime ($a_0\gg1$), the spectrum contains more energy in higher harmonics, which are emitted at lower frequencies due to the ponderomotive effect. This necessitates the calculation of scattered

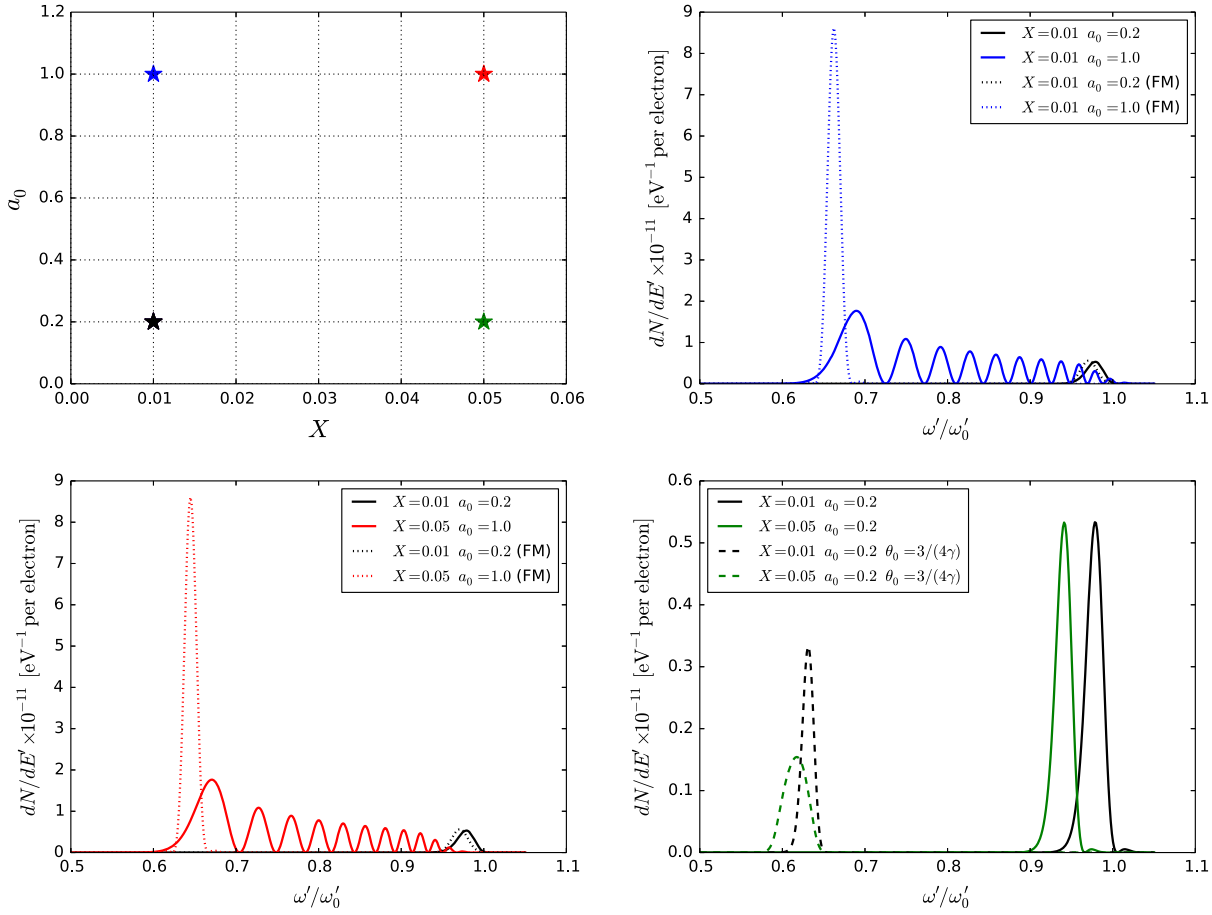

FIG. 3. Interplay between nonlinearities due to the high laser field ($a_0 \gg 0$) and due to the electron recoil ($X \gg 0$) and their influence on the scattered spectra. Top left: four cases sampling different regimes of the ICS parameter space—linear Thomson (black star); linear Compton (green star); nonlinear Thomson (blue star); and nonlinear Compton (red star). The remaining panels show the comparison between the single on-axis electron backscattered spectra for a linear Thomson case ($X = 0.01$, $E = 421$ MeV, $a_0 = 0.2$; black lines) and a nonlinear Thomson case ($X = 0.01$, $E = 421$ MeV, $a_0 = 1$; blue lines) (top right); a nonlinear Compton case ($X = 0.05$, $E = 2.1$ GeV, $a_0 = 1$; red lines) (bottom left); a linear Compton case ($X = 0.05$, $E = 2.1$ GeV, $a_0 = 0.2$; green lines) (bottom right). Also shown in the bottom right panel are the spectra at an oblique mean scattering angle of $\theta_0 = 3/(4\gamma)$ in the vertical direction. Dashed lines denote the spectra with FM and solid lines those without. Laser parameters are $\lambda = 800$ nm, $s \equiv \sigma_z/\lambda = 11.1$. The aperture used is in all of the simulations is 10 μrad.

radiation at a broader range of scattered frequencies, thereby incurring an additional computational costs. The computational cost is linearly proportional to the number of frequencies at which scattered spectrum is computed. While substantial, computational cost is rendered manageable even for distribution with long tails by massively parallelizing the code's execution.

III. RESULTS

Next we present specific cases calculated with the new model. Figure 3 presents the results of a spectrum calculation from a single, on-axis electron. Parameters are chosen as indicated by color and placement in the upper left plot. In the upper right plot, with relatively small Compton red shift, the radiation comes out as a single line (solid black) at $a_0 = 0.2$ and as a significantly broadened spectrum from the ponderomotive effect (solid blue) at $a_0 = 1$. When proper chirping is added to the incident laser pulse, a narrow line is recovered (dashed blue). The lower right plot indicated the Compton red-shifting that appears at higher electron recoil parameter $X \equiv 4E_L E_e/(m_e c^2)^2$ (green), where $E_L = \hbar c/\lambda_0$ is the photon energy, E_e is the electron energy, and m_e is the electron mass. Finally, the lower left plot illustrates the combined effect of Compton and ponderomotive red-shifting (solid red) and the fact that the ponderomotive red-shift can still be corrected by chirping to increase spectral density (dashed red).

Figure 4 presents the results of a spectrum calculation including emittance and with a ponderomotive red shift at $a_0 = 0.5$. Even at the lowest normalized emittance in the figure (green), the spectrum no longer clearly exhibits the interference dips evident in Fig. 3. Physically, the dips

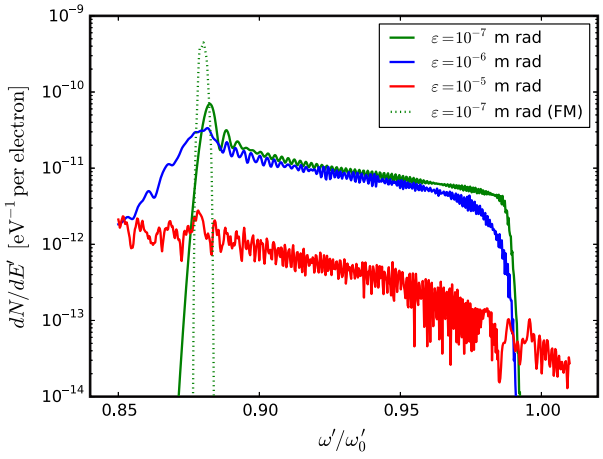

FIG. 4. Effects of emittance on spectral width and height. Backscattered spectra for the normalized emittance of $\epsilon = 10^{-7}$ m rad (green line), $\epsilon = 10^{-6}$ m rad (blue line), $\epsilon = 10^{-5}$ m rad (red line). Dashed green line represents the spectrum of the $\epsilon = 10^{-7}$ case with FM. Electron beam mean energy is $E = 360$ MeV, energy spread 6.5×10^{-4}; laser beam parameters are: $a_0 = 0.5$, $\lambda = 523$ nm, $s = \sigma_z/\lambda = 2295$. The aperture used is 1 μrad.

appear at different frequencies when emittance and energy spread are present and they are clearly washed out after integrating over the electron distribution. In the beginning, emittance acts to generate a low-energy tail in the spectrum (blue). When the emittance is large enough, the emitted line becomes so wide that the peak spectral density is reduced (red) [9].

Another interesting case is the ICS being built at ELI-NP [42]. The left-hand plot in Fig. 5 shows the calculated spectrum for the baseline parameters given in Table II. The two curves are spectra with the full Compton effect and for the Thomson limit where $\hbar = 0$ in the spectrum calculation. One observes a substantial red-shift in the spectrum due to electron recoil at ELI-NP parameters. Even more interesting is to exercise this new theory to compute spectra with a larger field strength in the incident laser pulse. In the center and right-hand plots, the maximum a_0 is 1 while all other parameters in the calculation are the same. Without beam chirping (solid line spectra), the spectrum is spread out from $\omega'/\omega'_0 = 1$ to $\omega'/\omega'_0 = 2/3$, as expected from the ponderomotive broadening of the spectral peak.

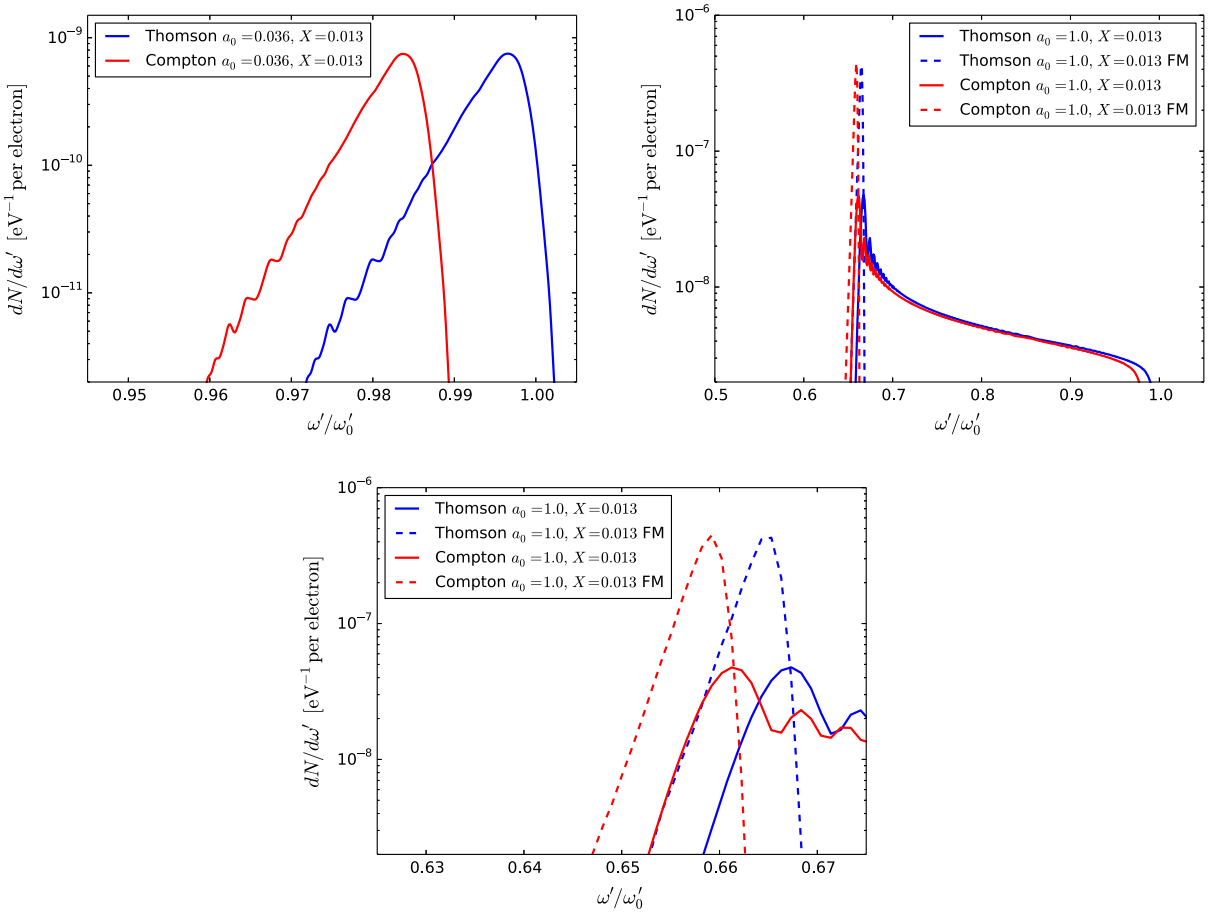

FIG. 5. Spectra for ELI-NP parameters, as listed in Table II. Left: Nominal parameters ($a_0 = 0.036$). Middle: $a_0 = 1.0$ with and without FM. Normalized to the maximum of the FM spectrum. Nonlinear subsidiary peaks arising from the non-negligible value of the laser field strength parameter a_0 are evident. Right: Middle panel enlarged around the main peaks. Note that the y range for the plots in the middle and the right are the same and are scaled by a factor of 1000 from the y range in the panel on the left.

TABLE II. Main parameters of electron and laser beams for ELI-NP project [42].

Quantity	Unit	Beam A
Electron beam mean energy E_e	MeV	360
Electron beam energy spread σ_E/E_e	MeV	0.234
Electron beam normalized horizontal emittance ε_x	mm mrad	0.65
Electron beam normalized vertical emittance ε_y	mm mrad	0.6
Electron beam horizontal size $\sigma_{e,x}$	μm	13.5
Electron beam vertical size $\sigma_{e,y}$	μm	13.5
Laser wavelength λ_0	μm	0.523
Laser energy E	J	1
Laser duration τ	ps	4
Laser waist $\sigma_{l,x} = \sigma_{l,y}$	μm	35
Field strength parameter a_0		0.036

When incident beam chirping is applied (dashed line spectra), we observed full recovery of the narrow spectral widths in the scattered radiation, even though because of emittance, the individual electrons are not perfectly (anti)aligned with the incident laser pulse. Applying chirping increases the peak spectral density by an order of magnitude. By calculating cases with higher electron beam emittance, it is shown that as long as the normalized emittance is less than 2×10^{-6} m rad, obtaining the full spectrum maximum in the scattered radiation is possible [33]. We believe our calculations using this new method are the first to quantify this possible limit to laser chirping.

For ELI-NP parameters, the efficacy of laser chirping has been evaluated as a function of a_0. The results are presented in Fig. 6. They indicate close to perfect recovery of the peak spectral density at $a_0 = 1$. This result is consistent with our

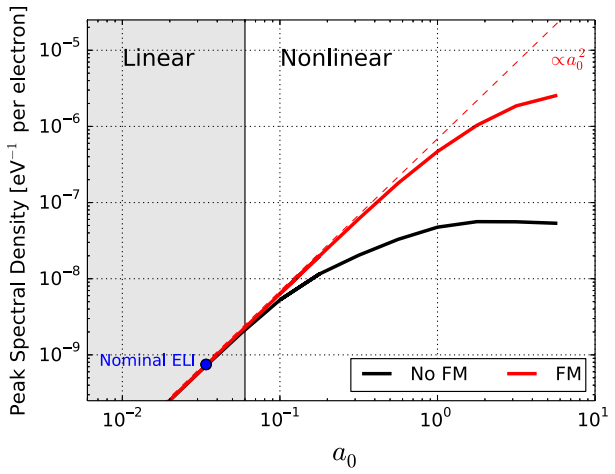

FIG. 6. Peak spectral density for ELI-NP parameters as the field strength parameter a_0 is varied. Black line denote non-FM spectra and red lines denote FM. Nominal ELI-NP parameters ($a_0 = 0.036$) is shown as a blue circle.

previous studies of chirping [36] but now includes the full Compton effect properly.

The new code, NLCS, subsumes ICS codes we developed earlier: SENSE [10] and NLTX [33] valid in the nonlinear Thomson regime and ICCS [37] in the linear Compton regime. Appendixes A and B show how the new methodology presented here reduces to the two special cases above: nonlinear Thomson in the limit of negligible electron recoil and linear Compton in the limit of the weak laser field. Therefore, benchmarks against experimental data of the nonlinear Thomson codes [10] and linear Compton code [37] reported earlier (or presently underway [43]) directly apply to benchmarking of the new NLCS code.

IV. CONCLUSION

In this study, we developed a new formalism for computing scattered spectra in the nonlinear Compton regime. It unifies the approaches previously used to separately investigate the nonlinear Thomson and the linear Compton regimes. The new approach, numerically implemented in the NLCS code is the first to properly model three features essential to the operation of ICS: (i) electron recoil at high electron beam energies, (ii) nonlinear behavior associated with high laser field strengths, and (iii) emittance in the realistic electron beam distributions. Adding an optional chirp to the frequencies of the laser pulse allows for a computational study of the advantages this novel technique.

In this paper, we have generated new results in cases where both Compton red-shifting and ponderomotive spectral broadening are significant. In addition, we have confirmed that the interference peaks associated with ponderomotive broadening tend to be washed out when the full emittance and energy spread of the beam are included in the calculation [39].

ACKNOWLEDGMENTS

This work is authored by Jefferson Science Associates, LLC under U.S. Department of Energy (DOE) Contract No. DE-AC05-06OR23177. The U.S. Government retains a nonexclusive, paid-up, irrevocable, world-wide license to publish or reproduce this manuscript for U.S. Government purposes. B. T. and E. J. are supported by NSF CAREER Grant No. 1847771. G. W. is supported by the U.S. National Science Foundation Research Experience for Undergraduates at Old Dominion University Grant No. 1950141.

APPENDIX A: REDUCTION TO NONLINEAR THOMSON

In this appendix, we show that the nonlinear Compton energy density spectrum reduces to the nonlinear Thomson energy density spectrum, i.e., Eq. (11) reduces to Eq. (6). The Thomson limit may be applied by taking the limit $\hbar \to 0$.

First, the Thomson limit will be applied to ω and ω', i.e., Eqs. (1) and (2):

$$\lim_{\hbar\to 0}\omega = \lim_{\hbar\to 0}\frac{\omega'(1-\boldsymbol{\beta}\cdot\hat{\boldsymbol{k}}')}{1-\boldsymbol{\beta}\cdot\hat{\boldsymbol{k}}-\frac{\hbar\omega'}{\gamma m_e c^2}(1-\hat{\boldsymbol{k}}\cdot\hat{\boldsymbol{k}}')} = \frac{\omega'(1-\beta\cdot\hat{\boldsymbol{k}}')}{1-\beta\cdot\hat{\boldsymbol{k}}}, \tag{A1}$$

and

$$\lim_{\hbar\to 0}\omega' = \lim_{\hbar\to 0}\frac{\omega(1-\boldsymbol{\beta}\cdot\hat{\boldsymbol{k}})}{1-\boldsymbol{\beta}\cdot\hat{\boldsymbol{k}}'+\frac{\hbar\omega}{\gamma m_e c^2}(1-\hat{\boldsymbol{k}}\cdot\hat{\boldsymbol{k}}')} = \frac{\omega(1-\beta\cdot\hat{\boldsymbol{k}})}{1-\beta\cdot\hat{\boldsymbol{k}}'}. \tag{A2}$$

Substituting Eq. (A1) into the portion of the Eq. (11) in the round brackets yields

$$\begin{aligned}&\frac{\omega'(1-\boldsymbol{\beta}\cdot\hat{\boldsymbol{k}}')}{2\omega(1-\boldsymbol{\beta}\cdot\hat{\boldsymbol{k}})}+\frac{\omega(1-\boldsymbol{\beta}\cdot\hat{\boldsymbol{k}})}{2\omega'(1-\boldsymbol{\beta}\cdot\hat{\boldsymbol{k}}')}-1\\ &=\frac{\omega'(1-\boldsymbol{\beta}\cdot\hat{\boldsymbol{k}}')}{2(1-\boldsymbol{\beta}\cdot\hat{\boldsymbol{k}})}\frac{1-\beta\cdot\hat{\boldsymbol{k}}}{\omega'(1-\beta\cdot\hat{\boldsymbol{k}}')}\\ &\quad+\frac{(1-\boldsymbol{\beta}\cdot\hat{\boldsymbol{k}})}{2\omega'(1-\boldsymbol{\beta}\cdot\hat{\boldsymbol{k}}')}\frac{\omega'(1-\beta\cdot\hat{\boldsymbol{k}}')}{1-\beta\cdot\hat{\boldsymbol{k}}}-1=\frac{1}{2}+\frac{1}{2}-1=0.\end{aligned} \tag{A3}$$

Similarly, combining Eqs. (1) and (2), we arrive at the ratio of the scattered to incoming frequencies

$$\frac{\omega'}{\omega} = \frac{1-\beta\cdot\hat{\boldsymbol{k}}-\frac{\hbar\omega'}{\gamma m_e c^2}(1-\hat{\boldsymbol{k}}\cdot\hat{\boldsymbol{k}}')}{(1-\beta\cdot\hat{\boldsymbol{k}}')}, \tag{A4}$$

which, after applying the Thomson limit, becomes

$$\lim_{\hbar\to 0}\frac{\omega'}{\omega} = \frac{1-\beta\cdot\hat{\boldsymbol{k}}}{1-\beta\cdot\hat{\boldsymbol{k}}'}. \tag{A5}$$

Solving for the derivative of ω with respect to ω', we obtain

$$\begin{aligned}\frac{d\omega}{d\omega'} &= \frac{d}{d\omega'}\left[\frac{\omega'(1-\beta\cdot\hat{\boldsymbol{k}}')}{1-\beta\cdot\hat{\boldsymbol{k}}-\frac{\hbar\omega'}{\gamma m_e c^2}(1-\hat{\boldsymbol{k}}\cdot\hat{\boldsymbol{k}}')}\right]\\ &=\frac{(1-\beta\cdot\hat{\boldsymbol{k}}')}{1-\beta\cdot\hat{\boldsymbol{k}}-\frac{\hbar\omega'}{\gamma m_e c^2}(1-\hat{\boldsymbol{k}}\cdot\hat{\boldsymbol{k}}')}\\ &\quad-\frac{\omega'(1-\beta\cdot\hat{\boldsymbol{k}}')}{(1-\beta\cdot\hat{\boldsymbol{k}}-\frac{\hbar\omega'}{\gamma m_e c^2}(1-\hat{\boldsymbol{k}}\cdot\hat{\boldsymbol{k}}'))^2}\frac{\hbar(1-\hat{\boldsymbol{k}}\cdot\hat{\boldsymbol{k}}')}{\gamma m_e c^2}.\end{aligned} \tag{A6}$$

Applying the Thomson limit to the derivative, it follows

$$\lim_{\hbar\to 0}\frac{d\omega}{d\omega'} = \frac{1-\beta\cdot\hat{\boldsymbol{k}}'}{1-\beta\cdot\hat{\boldsymbol{k}}}. \tag{A7}$$

Finally, multiply Eqs. (A5) and (A7) to get unity, $[(\omega'/\omega)(d\omega/d\omega')]=1$. Equation (11) becomes

$$\frac{\mathrm{d}^2E'_{\mathrm{tot}}}{\mathrm{d}\omega'\mathrm{d}\Omega} = \frac{\mathrm{d}^2E'_{\boldsymbol{\varepsilon}'}}{\mathrm{d}\omega'\mathrm{d}\Omega}. \tag{A8}$$

The last step to show that NLCS can reduce to the nonlinear Thomson regime is to show that $\omega''\to\omega'$ in the Thomson limit. The Compton-shifted nonlinear scattered frequency is defined as [37]

$$\omega'' = \frac{\omega'(1-\boldsymbol{\beta}\cdot\hat{\boldsymbol{k}})}{1-\boldsymbol{\beta}\cdot\hat{\boldsymbol{k}}-\frac{\hbar\omega'}{\gamma m_e c^2}(1-\hat{\boldsymbol{k}}\cdot\hat{\boldsymbol{k}}')}. \tag{A9}$$

Note that $-(\hbar\omega'/\gamma m_e c^2)(1-\hat{\boldsymbol{k}}\cdot\hat{\boldsymbol{k}}')$ accounts for the Compton recoil. Now apply the Thomson limit to obtain

$$\lim_{\hbar\to 0}\omega'' = \frac{\omega'(1-\boldsymbol{\beta}\cdot\hat{\boldsymbol{k}})}{1-\boldsymbol{\beta}\cdot\hat{\boldsymbol{k}}} = \omega'. \tag{A10}$$

All of these steps are how NLCS reduces to NLTX and how it can simulate the Thomson regime exactly like NLTX. Furthermore, NLCS must also be able to reduce to linear Compton, i.e., NLCS must reduce to ICCS.

APPENDIX B: REDUCTION TO LINEAR COMPTON

In this appendix, we show that the nonlinear Compton energy density spectrum reduces to the linear Compton energy density spectrum, i.e., Eq. (11) reduces to Eq. (3).The limit for the linear Compton regime is $a_0 \ll 1$. From the definition of D_1 and D_2 in Eq. (7), the amplitude of $\tilde{A}$ is a_0, so this implies that $D_1 \gg D_2$. In the linear limit, the nonlinear Thomson element in Eq. (6) becomes

$$\begin{aligned}\lim_{a_0\ll 1}\frac{\mathrm{d}^2E'_{\boldsymbol{\varepsilon}'}}{\mathrm{d}\omega'\mathrm{d}\Omega} &= \frac{e^2\omega'^2}{16\pi^3\epsilon_0 c^3}|D_1(\omega'')|^2\left|(\boldsymbol{\varepsilon}\cdot\boldsymbol{\varepsilon}')+\frac{(\boldsymbol{\beta}\cdot\boldsymbol{\varepsilon})(\hat{\boldsymbol{k}}\cdot\boldsymbol{\varepsilon}')}{(1-\boldsymbol{\beta}\cdot\hat{\boldsymbol{k}})}\right.\\ &\quad\left.-\frac{(\boldsymbol{\beta}\cdot\boldsymbol{\varepsilon}')(\boldsymbol{\beta}\cdot\boldsymbol{\varepsilon})(1-\hat{\boldsymbol{k}}\cdot\hat{\boldsymbol{k}}')}{(1-\boldsymbol{\beta}\cdot\hat{\boldsymbol{k}})(1-\boldsymbol{\beta}\cdot\hat{\boldsymbol{k}}')}+\frac{(\boldsymbol{\beta}\cdot\boldsymbol{\varepsilon}')(\hat{\boldsymbol{k}}\cdot\boldsymbol{\varepsilon})}{(1-\boldsymbol{\beta}\cdot\hat{\boldsymbol{k}}')}\right|^2\\ &=\frac{e^2\omega'^2}{16\pi^3\epsilon_0 c^3}|D_1(\omega'')|^2|\varepsilon_b\cdot\varepsilon'_b|^2.\end{aligned} \tag{B1}$$

Next, substitute Eq. (B1) into Eq. (6)

$$\begin{aligned}\frac{\mathrm{d}^2E'_{\mathrm{tot}}}{\mathrm{d}\omega'\mathrm{d}\Omega} &= \frac{e^2\omega'^2}{32\pi^3\epsilon_0 c^3}|D_1(\omega'')|^2\left[\frac{\omega'(1-\boldsymbol{\beta}\cdot\hat{\boldsymbol{k}}')}{2\omega(1-\boldsymbol{\beta}\cdot\hat{\boldsymbol{k}})}\right.\\ &\quad\left.+\frac{\omega(1-\boldsymbol{\beta}\cdot\hat{\boldsymbol{k}})}{2\omega'(1-\boldsymbol{\beta}\cdot\hat{\boldsymbol{k}}')}-1+2|\boldsymbol{\varepsilon}_b\cdot\boldsymbol{\varepsilon}'_b|^2\right]\left[\frac{\omega'}{\omega}\frac{d\omega}{d\omega'}\right].\end{aligned} \tag{B2}$$

Now it will be shown that D_1 in Eq. (7) reduces to the Fourier transform for the electric field. This will produce the energy density spectrum equation for linear Compton scattering. For the same reason that $D_1 \gg D_2$, $\Phi(\xi')$ in Eq. (7) reduces to the exponential argument in the Fourier transform in the linear limit. For $a_0 \ll 1$, the following is true

$$\xi' \gg \frac{1}{\gamma(1-\boldsymbol{\beta}\cdot\hat{\boldsymbol{k}})}\int_{-\infty}^{\xi'}\tilde{A}(\xi')e^{i\Phi(\xi')}\mathrm{d}\xi'$$

$$\gg \frac{1}{\gamma^2(1-\boldsymbol{\beta}\cdot\hat{\boldsymbol{k}})^2}\int_{-\infty}^{\xi'}\frac{\tilde{A}^2(\xi')}{2}e^{i\Phi(\xi')}\mathrm{d}\xi'. \tag{B3}$$

Therefore the phase argument $\Phi(\xi')$, Eq. (7) becomes

$$\lim_{a_0\ll 1}\Phi(\xi') = \frac{\omega(\omega')}{c}\xi'. \tag{B4}$$

Notice the term in the first set of brackets in Eq. (B2) is similar to the Klein-Nishina cross section in Eq. (4). The energy density spectrum for the linear Compton regime may be written in terms of Eq. (4):

$$\frac{\mathrm{d}^2E'_{\mathrm{tot}}}{\mathrm{d}\omega'\mathrm{d}\Omega} = \frac{e^2\omega'^2}{32\pi^3\epsilon_0c^3}|D_1(\omega'')|^2\frac{\gamma^2(1-\boldsymbol{\beta}\cdot\hat{\boldsymbol{k}})^2}{r_e^2}\left(\frac{\omega}{\omega'}\right)^2\frac{\mathrm{d}\sigma}{\mathrm{d}\Omega} \times\left[\frac{\omega'}{\omega}\frac{d\omega}{d\omega'}\right]. \tag{B5}$$

The argument of the modulus squared may be rewritten as

$$\frac{\mathrm{d}^2E'_{\mathrm{tot}}}{\mathrm{d}\omega'\mathrm{d}\Omega} = \frac{e^2}{32\pi^3\epsilon_0c^3}\left|\frac{D_1(\omega'')\gamma(1-\boldsymbol{\beta}\cdot\hat{\boldsymbol{k}})\omega}{r_e}\right|^2\frac{\mathrm{d}\sigma}{\mathrm{d}\Omega}\left[\frac{\omega'}{\omega}\frac{d\omega}{d\omega'}\right]. \tag{B6}$$

The argument inside of the modulus squared is equal to the Fourier transform of the electric field $\tilde{E}(\omega(\omega')/c)$

$$\begin{aligned}\frac{D_1(\omega'')\gamma(1-\boldsymbol{\beta}\cdot\hat{\boldsymbol{k}})}{r_e} &= \frac{\omega}{c}\int\tilde{A}(\xi')e^{i\xi'\frac{\omega}{c}}\mathrm{d}\xi' \\ &= \frac{\omega e}{mc^2}\int A(\xi')e^{i\xi'\frac{\omega}{c}}\mathrm{d}\xi' \\ &= \frac{e}{mc^2}\tilde{E}\left(\frac{\omega(\omega')}{c}\right).\end{aligned} \tag{B7}$$

Substituting Eq. (B8) back into Eq. (B6) yields

$$\frac{\mathrm{d}^2E'_{\mathrm{tot}}}{\mathrm{d}\omega'\mathrm{d}\Omega} = \frac{e^4}{32\pi^3\epsilon_0c^5r_e^2m^2}\left|\tilde{E}\left(\frac{\omega(\omega')}{c}\right)\right|^2\frac{\mathrm{d}\sigma}{\mathrm{d}\Omega}\left[\frac{\omega'}{\omega}\frac{d\omega}{d\omega'}\right]. \tag{B8}$$

The electron radius r_e is defined in terms of the constants used in Eq. (B8):

$$r_e = \frac{e^2}{4\pi\epsilon_0mc^2}. \tag{B9}$$

After substituting Eq. (B9) into Eq. (B8), the energy density spectrum for ICCS, Eq. (3), is recovered:

$$\frac{\mathrm{d}^2E'_{\mathrm{tot}}}{\mathrm{d}\omega'\mathrm{d}\Omega} = \frac{\epsilon_0}{2\pi c}\left|\tilde{E}\left(\frac{\omega(\omega')}{c}\right)\right|^2\frac{\mathrm{d}\sigma}{\mathrm{d}\Omega}\left[\frac{\omega'}{\omega}\frac{d\omega}{d\omega'}\right].$$

[1] G. A. Krafft and G. Priebe, Rev. Accel. Sci. Technol. **03**, 147 (2010).
[2] B. Günther, R. Gradl, C. Jud, E. Eggl, J. Huang, S. Kulpe, K. Achterhold, B. Gleich, M. Dierolf, and F. Pfeiffer, J. Synchrotron Radiat. **27**, 1395 (2020).
[3] W. S. Graves, J. Bessuille, P. Brown, S. Carbajo, V. Dolgashev, K. H. Hong, E. Ihloff, B. Khaykovich, H. Lin, K. Murari, E. A. Nanni, G. Resta, S. Tantawi, L. E. Zapata, F. X. Kärtner, and D. E. Moncton, Phys. Rev. ST Accel. Beams **17**, 120701 (2014).
[4] C. Sun and Y. K. Wu, Phys. Rev. ST Accel. Beams **14**, 044701 (2011).
[5] O. Adriani *et al.*, ELI-NP-GBS Technical Design Report, http://arxiv.org/ftp/arxiv/papers/1407/1407.3669.pdf, 2014.
[6] D. Micieli, I. Drebot, A. Bacci, E. Milotti, V. Petrillo, M. Rossetti Conti, A. R. Rossi, E. Tassi, and L. Serafini, Phys. Rev. Accel. Beams **19**, 093401 (2016).
[7] K. Deitrick, C. Franck, G. Hoffstaetter, B. Muratori, P. Williams, G. Krafft, B. Terzić, J. Crone, and H. Owen, Phys. Rev. Accel. Beams **24**, 050701 (2021).
[8] P. Chen, G. Horton-Smith, T. Ohgaki, A. W. Weidemann, and K. Yokoya, Nucl. Instrum. Methods Phys. Res., Sect. A **355**, 107 (1995). Gamma-Gamma Colliders.
[9] N. Ranjan, B. Terzić, G. A. Krafft, V. Petrillo, I. Drebot, and L. Serafini, Phys. Rev. Accel. Beams **21**, 030701 (2018).
[10] B. Terzić, A. Brown, I. Drebot, T. Hagerman, E. Johnson, G. A. Krafft, C. Maroli, V. Petrillo, and M. Ruijter, Europhys. Lett. **126**, 12003 (2019).
[11] E. Esarey, S. Ride, and P. Sprangle, Phys. Rev. E **48**, 3003 (1993).
[12] F. V. Hartemann, J. R. Van Meter, A. L. Troha, E. C. Landahl, N. C. Luhmann, H. A. Baldis, A. Gupta, and A. K. Kerman, Phys. Rev. E **58**, 5001 (1998).
[13] F. V. Hartemann, Phys. Plasmas **5**, 2037 (1998).
[14] G. A. Krafft, Phys. Rev. Lett. **92**, 204802 (2004).
[15] C. Brau, Phys. Rev. ST Accel. Beams **7**, 020701 (2004).
[16] I. Ghebregziabher, B. A. Shadwick, and D. Umstadter, Phys. Rev. ST Accel. Beams **16**, 030705 (2013).
[17] B. Terzić, K. Deitrick, A. S. Hofler, and G. A. Krafft, Phys. Rev. Lett. **112**, 074801 (2014).
[18] S. G. Rykovanov, C. G. R. Geddes, C. B. Schroeder, E. Esarey, and W. P. Leemans, Phys. Rev. Accel. Beams **19**, 030701 (2016).
[19] B. Terzić and G. A. Krafft, Phys. Rev. Accel. Beams **19**, 098001 (2016).
[20] B. Terzić, J. McKaig, E. Johnson, T. Dharanikota, and G A. Krafft, Phys. Rev. Accel. Beams **24**, 094401 (2021).
[21] D. Seipt, S. G. Rykovanov, A. Surzhykov, and S. Fritzsche, Phys. Rev. A **91**, 033402 (2015).
[22] D. Seipt and B. Kämpfer, Phys. Rev. A **83**, 022101 (2011).
[23] F. Albert, S. G. Anderson, D. J. Gibson, R. A. Marsh, C. W. Siders, C. P. J. Barty, and F. V. Hartemann, Phys. Plasmas **18**, 013108 (2011).

[24] F. V. Hartemann, W. J. Brown, D. J. Gibson, S. G. Anderson, A. M. Tremaine, P. T. Springer, A. J. Wootton, E. P. Hartouni, and C. P. J. Barty, Phys. Rev. ST Accel. Beams **8**, 100702 (2005).
[25] C. P. Ridgers, J. G. Kirk, R. Duclous, T. G. Blackburn, C. S. Brady, K. Bennett, T. D. Arber, and A. R. Bell, J. Comput. Phys. **260**, 273 (2014).
[26] X. Artru, Phys. Rev. Accel. Beams **22**, 050705 (2019).
[27] Y. Li, R. Shaisultanov, K. Z. Hatsagortsyan, F. Wan, C. H. Keitel, and J. Li, Phys. Rev. Lett. **122**, 154801 (2019).
[28] A. Di Piazza, Phys. Rev. Lett. **113**, 040402 (2014).
[29] A. Di Piazza, Phys. Rev. D **103**, 076011 (2021).
[30] A. Gonoskov, S. Bastrakov, E. Efimenko, A. Ilderton, M. Marklund, I. Meyerov, A. Muraviev, A. Sergeev, I. Surmin, and E. Wallin, Phys. Rev. E **92**, 023305 (2015).
[31] M. Vranic, T. Grismayer, R. A. Fonseca, and L. O. Silva, New J. Phys. **18**, 073035 (2016).
[32] F. Mackenroth, N. Kumar, N. Neitz, and C. H. Keitel, Phys. Rev. E **99**, 033205 (2019).
[33] E. Johnson, E. Breen, G. A. Krafft, and B. Terzić, Phys. Rev. Accel. Beams **25**, 054401 (2022).
[34] C. Maroli, V. Petrillo, I. Drebot, L. Serafini, B. Terzić, and G. A. Krafft, J. Appl. Phys. **124**, 063105 (2018).
[35] F. Mackenroth, A. R. Holkundkar, and H. P. Schlenvoigt, New J. Phys. **21**, 123028 (2019).
[36] B. Terzić, C. Reeves, and G. A. Krafft, Phys. Rev. Accel. Beams **19**, 044403 (2016).
[37] G. Krafft, E. Johnson, K. Deitrick, B. Terzić, R. Kelmar, T. Hodges, W. Melnitchouk, and J. Delayen, Phys. Rev. Accel. Beams **19**, 121302 (2016).
[38] C. Maroli, V. Petrillo, I. Drebot, L. Serafini, B. Terzić, and G. Krafft, J. Appl. Phys. **124**, 063105 (2018).
[39] M. A. Valialshchikov, V. Yu. Kharin, and S. G. Rykovanov, Phys. Rev. Lett. **126**, 194801 (2021).
[40] The Python programming language, http://www.python.org.
[41] Cython: C-extensions for Python, http://www.cython.org.
[42] C. Vaccarezza *et al.*, in *Proceedings of the 3rd International Particle Accelerator Conference, New Orleans, LA, 2012* (IEEE, Piscataway, NJ, 2012), p. 1086.
[43] B. Günther, B. Terzić, M. Dierolf, G. Krafft, and F. Pfeiffer (to be published).